Supporting Information

Lead-Free Layered Halide Double Perovskites with Aromatic Organic Cations for Resistive Switching Memories and Artificial Synapses

Mubashir Mushtaq Ganaie[1,2,3], Mahdi Mohammadi[4], Michalis Loizos[5], Konstantinos Rogdakis[5,6],

Rashid M. Ansari[1], Gianluca Bravetti[3], Maryam Ghasemi[7], Mohammad Reza Golobostanfard[7],

Kishan Kumar[1], Shahab Ahmad[1], Satyajit Sahu[1], Emmanuel Kymakis[5,6], Wolfgang Tress[4],

Jovana V. Milić[3,7*], Mahesh Kumar[2*]

[1]Department of Physics, Indian Institute of Technology Jodhpur, Jodhpur 342030, India; [2]Department of Electrical Engineering, Indian Institute of Technology Jodhpur, Jodhpur 342030, India; [3]Adolphe Merkle Institute, University of Fribourg, Fribourg 1700, Switzerland; [4]Institute of Computational Physics, Zurich University of Applied Sciences (ZHAW), Winterthur, 8400 Switzerland; [5]Department of Electrical & Computer Engineering, Hellenic Mediterranean University (HMU), Heraklion 71410, Crete, Greece; [6]Institute of Emerging Technologies (i-EMERGE) of HMU Research Center, Heraklion 71410, Crete, Greece; [7]Department of Chemistry, University of Turku, Turku 20500, Finland. Correspondence e-mail: jovana.milic@unifr.ch; mkumar@iitj.ac.in

Table of Contents

Experimental Section

Synthesis of Perovskite Materials: Layered double perovskites based on 1,4-phenylenedimethylammonium (PDMA) and benzylammonium (BzA) of $(PDMA)_2AgBiX_8$ and $(BzA)_4AgBiX_8$ (X = I, Br) composition were prepared by mechanosynthesis.[1,2] Stoichiometric amounts of the organic halide salts ($PDMAI_2$, $PDMABr_2$, BzI, BzBr), silver halides (AgI, AgBr), and bismuth halides (BiI_3, $BiBr_3$) were mixed in an inert nitrogen atmosphere within a glovebox and milled using a Retsch MM-400 high-energy ball mill operating at 25 Hz for 30 min. The milling was performed in 5 mL agate jars with two stainless steel balls (5 mm diameter). Post milling, the as-prepared powders were thermally annealed at 150 °C for 10 min.

Deposition of Perovskite Thin Films: The active layers were prepared by dissolving the synthesized perovskite powders in a mixed solvent of dimethylformamide (DMF): dimethyl sulfoxide (DMSO). For iodide-based compositions, a 4:1 volumetric ratio was used, whereas bromide systems employed a 1:1 ratio, yielding 0.4 M solutions. Prior to film deposition, fluorine-doped tin oxide (FTO) glass substrates were ultrasonicated sequentially in Vim solution, isopropanol, and ethanol for 10 min each. After nitrogen drying, the substrates were treated with UV-ozone for 10 min. Films were spin-coated using a two-step program: 1000 rpm for 10 s followed by 4000 rpm for 20 s. Subsequently, the deposited layers were annealed at 150 °C for 10 min inside an argon-filled glovebox.

Preparation of Electron and Hole Transport Layers: For electron transport layers (ETLs), SnO_2 films were deposited by two distinct methods. RF sputtering was carried out at room temperature under a base vacuum of 2.5×10^{-6} mbar, using an RF power of 50 W, argon gas flow of 30 SCCM, and a working pressure of 2×10^{-2} mbar. The target-substrate distance was fixed at 5 cm, and deposition for 8 min yielded a 50 nm SnO_2 layer. Alternatively, for solution-based deposition, commercial SnO_2 colloid was diluted in DI water (1:4) and spin-coated at 3000 rpm for 30 s, followed by annealing at 150 °C for 30 min. For the hole transport layer (HTL), 2,2′,7,7′-Tetrakis[N,N-di(4-methoxyphenyl)amino]-9,9′-spiro-bifluorene(Spiro-OMeTAD) (100 mg) was dissolved in 1.09 mL chlorobenzene and doped with 24.5 μL Li-TFSI (1.8 mol/L in acetonitrile) and 43 μL of 4-*tert*-butylpyridine (tBP). The resulting solution was spin-coated onto the perovskite films at 4000 rpm for 20 s.

Device Fabrication: Devices were fabricated in both conventional metal-insulator-metal (MIM) configurations and in solar cell-inspired architectures incorporating charge transport

layers. Fluorine-doped tin oxide (FTO) coated glass substrates served as the bottom electrode. In solar cell-type structures, a compact SnO_2 layer was deposited either via RF sputtering (50 nm) or spin-coating as the electron transport layer (ETL). Layered double perovskite thin films were then deposited as the active resistive switching medium. For hole transport, a Spiro-OMeTAD layer was spin-coated atop the perovskite to serve as the hole transport layer (HTL). Circular top contacts of Ag, Au, or Al were thermally evaporated through a shadow mask (1.8 mm diameter) at a deposition rate of 0.1 Å/s to achieve a thickness of 100 nm. In selected cases, bilayer electrodes, comprising 10 nm Ag followed by 100 nm Au, were also employed.

Device characterization: Surface and morphological analyses were carried out using a Thermo Scientific Apreo 2 FESEM. Elemental composition and spatial distribution were examined via energy-dispersive X-ray spectroscopy (EDX) using a Zeiss EVO 18 SEM equipped with an Oxford Instruments EDS system. TEM was recorded on Thermo Fisher, Talos F200i. Sample for TEM was prepared by drop casting the solution (0.05 M in DMF: DMSO)) on the grid followed by heating at 150 C for 20 minutes. Impedance spectroscopy was performed using a HIOKI IM3536 LCR meter. THORLABS UV Mounted LED 365nm was used to produce UV light, to measure the photo-response behaviour of the devices. The light pulses were generated using chopper with 0.4 Hz frequency. The photoelectric performance was measured using Keithley 2634B SMU. To exclude the impact of ambient light, all optical measurements were obtained at room temperature in an optically sealed laboratory. All solar cell device characterization took place on unencapsulated devices at room temperature. The J - V curves under illumination were acquired with a Sun 3000 Class AAA solar simulator from Abet Technologies equipped with a Xenon lamp. The lamp intensity was calibrated to AM1.5G (100 mW/cm^2) with a ReRa Solutions silicon cell filtered with KG5 glass. The illuminated area is defined with a non-reflective metal shadow mask of 0.101 cm^2, avoiding the effects of scattered light. No previous light soaking or bias has been applied to the devices prior to J - V characterization.

Electrical characterization of the devices was carried out using a Keithley 2634B source measurement unit (SMU). The voltage bias was applied to the top electrode while the FTO bottom electrode was grounded, with a compliance current of 100 mA employed throughout the measurements to prevent hard breakdown and regulate filament formation. A scan rate of 773 mV/s was used for voltage sweeping. For each composition, two identical devices were fabricated, and both silver and gold top electrodes were deposited on separate halves of the same substrate. This design allowed us to directly compare

electrode-dependent effects while minimizing device-to-device variation, thereby ensuring more consistent and reliable comparisons.

Testing protocol: The measurement protocol involved an initial optimization step to determine the appropriate set and reset voltages for each device. In general, the protocol begins by probing a single cell (dot/electrode) to identify the switching window and determine optimal set/reset voltages. The sweeps typically start from 0 V → small positive bias (e.g., +0.5 V) → back to 0 V. If no switching to LRS is observed, the positive bias is increased stepwise (e.g., +1.0 V, +1.5 V, etc.). If even after increasing the positive bias no transition occurs, the protocol is then repeated on the negative side, with sweeps 0 V → negative bias → back to 0 V, stepwise increasing the magnitude until a clear set process is observed. This ensures that both possible polarities are systematically tested before defining the optimal switching window.

In our case, in non-volatile devices, the set process was always observed under negative bias and the reset under positive bias. The sweeps were therefore applied in the order 0 V → negative bias → back to 0 V, which switched the device to LRS. To return the device to HRS, a subsequent sweep 0 V → positive bias → back to 0 V was required. If the initial negative bias was insufficient to induce switching, the voltage was gradually increased stepwise (e.g., from -0.5V to −1 V) until a complete set to LRS was achieved. Similarly, the reset voltage was optimized by increasing the positive bias stepwise until a complete return to HRS was observed. In this way, the optimal set and reset voltages were established for each device.

Once these conditions were identified, cycling was performed continuously by repeating sweeps in the sequence 0 V → negative bias → back to 0 V → 0 V → positive bias → back to 0 V or positive bias → 0 V → negative bias → back to 0 V → 0 V → positive bias. This confirmed stable bipolar non-volatile switching, with negative sweeps acting as set operations and positive sweeps acting as reset operations.

In contrast, volatile devices behaved differently. When sweeps were applied in either direction, 0 V → negative bias → back to 0 V or 0 V → positive bias → back to 0 V, the device switched to LRS but did not retain this state, instead relaxing spontaneously to HRS. After a negative sweep, relaxation occurred within minutes, whereas following a positive sweep, the relaxation could take hours. If a second sweep (0 V → negative bias → back to 0 V) was applied immediately without delay, the device retraced the LRS path because it had insufficient time to relax. However, if the device was allowed to rest for

~10 minutes before reapplying the same sweep, it was again found in HRS and then switched once more to LRS. The same effect was observed for the positive side.

In volatile devices, an additional feature was observed: when a continuous scan was applied in the sequence 0 V → negative bias → back to 0 V → 0 V → +0.8 V → back to 0 V, the device reset to HRS under this small positive voltage (+0.8 to +1.0 V). A similar response was seen when the order was reversed, i.e., +0.8 V → 0 V → negative bias → back to 0 V → 0 V → +0.8 V. Thus, in volatile switching, both positive and negative sweeps could act as set operations, while the reset was either spontaneous (via conductance drift) or assisted by a small positive bias.

Due to the exploratory nature of 1st step, the device used in this phase often degrades after repeated cycling or parameter sweeping. Once optimal parameters are identified, these are then applied to multiple separate cells across the two identical devices. Each cell is subjected to repeated cycling (typically 10 cycles), and the switching characteristics are recorded. Based on this dataset, a switching behavior is classified as representative if it is observed in more than 50% of the cells tested. Halide perovskites generally exhibit higher device-to-device variability as compared to oxides, and a 50% threshold is used to define dominant behavior. In Figure 2, representative single cycles provide a qualitative overview of the diverse switching behaviors observed across different compositions and electrode configurations, particularly the contrast between volatile and non-volatile responses, and the effect of transport layers on switching symmetry without overcomplicating the visual layout. Data shown in Figures 3 and 5 represent complete results for non-volatile and volatile cases, respectively. Additional supporting data for volatile switching in devices with spin-coated SnO_2 are included in Figure S17. In volatile cases (Figure 2), forward and reverse branches of the sweeps are plotted together to capture the complete loop in a single panel. In contrast, in Figure 5 the forward and reverse sweeps are shown with different colors and each branch separately, to more clearly illustrate the switching dynamics.

Device stability varied significantly between materials. The failure modes also varied. Some devices failed only after few cycles (even less than 10 cycles). Some fail at retention after the cycling. Some during WRER. and the most stable system $(BzA)_4AgBiBr_8$ survived extended testing and were stable enough to support synaptic experiments.

Further, during fabrication and testing of PDMA-I devices, it was observed that silver and aluminum electrodes began degrading over time, disappearing from the surface (Figure S20). The degradation was more pronounced in PDMA-based compositions than in BzA systems, suggesting a higher intrinsic reactivity of PDMA-based perovskites with silver. To prevent this

degradation, a 10 nm silver layer beneath a 100 nm gold electrode was introduced, with the intention that gold would act as a protective cap against oxidation. Based on this, we initially expected the device to exhibit non-volatile switching. But later we realized that even though some devices were not yet exposed to air but still their electrode disappeared. Further, during data analysis, it became apparent that the silver layer was likely reacting with the perovskite itself, forming AgI, rather than simply oxidizing in air. In the Au/Ag device, this reaction likely consumed most or all of the thin Ag layer, leaving the inert Au interface directly exposed to the perovskite. Since gold does not participate in filament stabilization, the device ultimately displayed volatile switching behavior.

Supplementary data
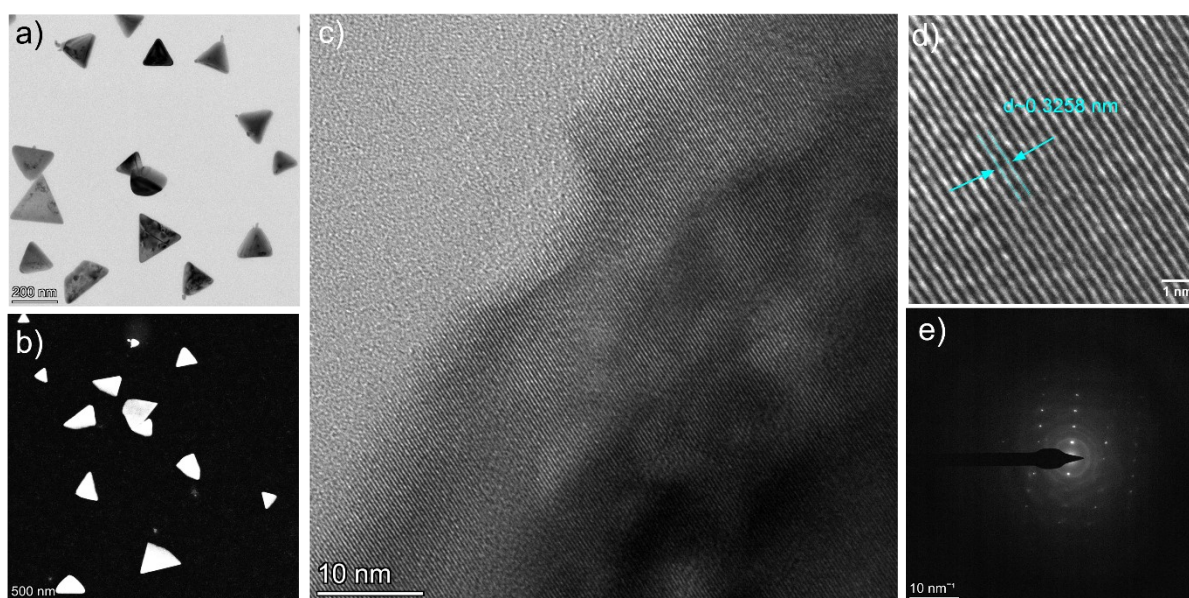
Figure S1. Transmission electron microscopy (TEM) analysis of (BzA)$_4$AgBiBr$_8$ a) Bright field TEM micrograph. b) High-angle annular dark-field TEM (HAADF-TEM). c-d) High resolution TEM (HRTEM) images e) Selective area electron diffraction (SAED) pattern.
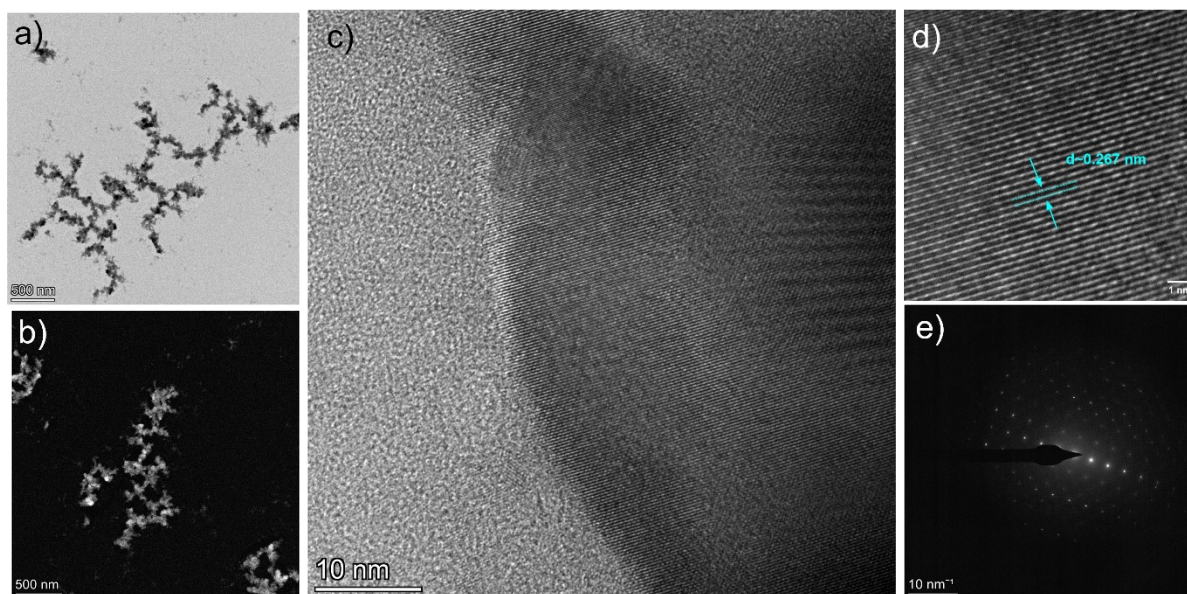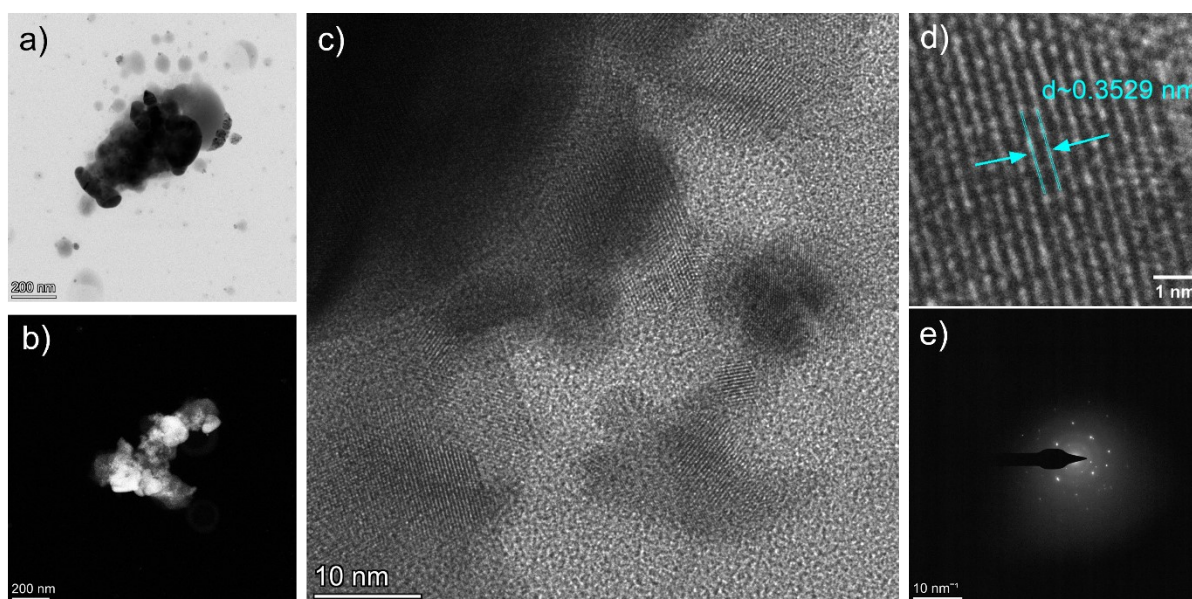
Figure S2. Transmission electron microscopy (TEM) analysis of $(PDMA)_2AgBiBr_8$. a) Bright field TEM micrograph. b) High-angle annular dark-field TEM (HAADF-TEM). c-d) High resolution TEM (HRTEM) images e) Selective area electron diffraction (SAED) pattern.

Figure S3. Transmission electron microscopy (TEM) analysis of $(PDMA)_2AgBiI_8$. a) Bright field TEM micrograph. b) High-angle annular dark-field TEM (HAADF-TEM). c-d) High resolution TEM (HRTEM) images e) Selective area electron diffraction (SAED) pattern.
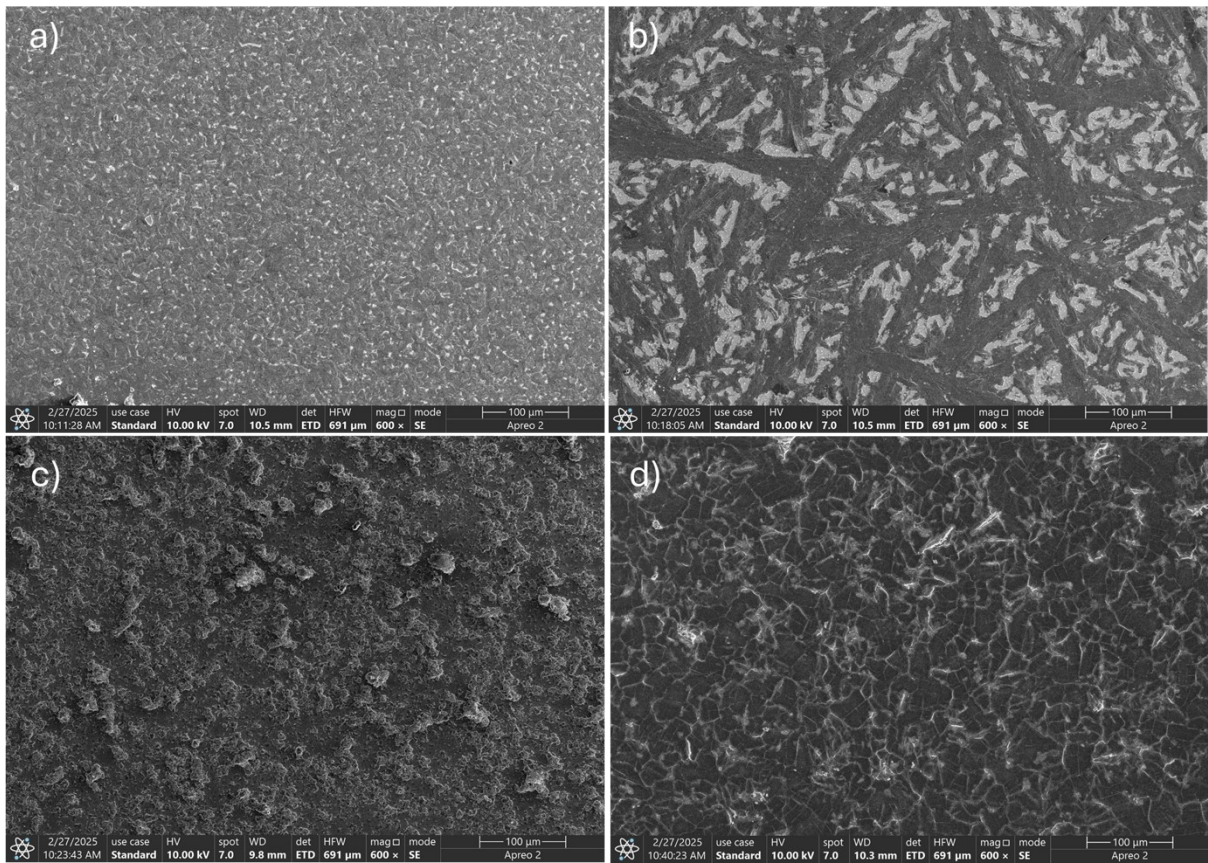
Figure S4. FESEM images of a) $(PDMA)_2AgBiI_8$ b) $(BzA)_4AgBiI_8$ c) $(PDMA)_2AgBiBr_8$ d) $(BzA)_4AgBiBr_8$ double perovskite thin films.

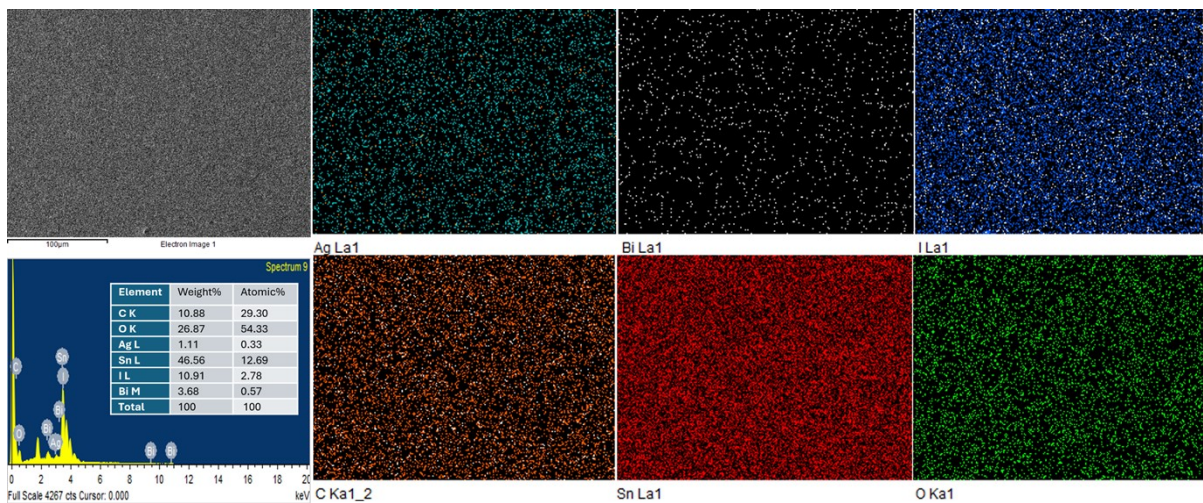**Figure S5**. Energy dispersive spectroscopy (EDS). SEM image, elemental mapping, and EDX spectrum of $(PDMA)_2AgBiI_8$ double perovskite thin film.
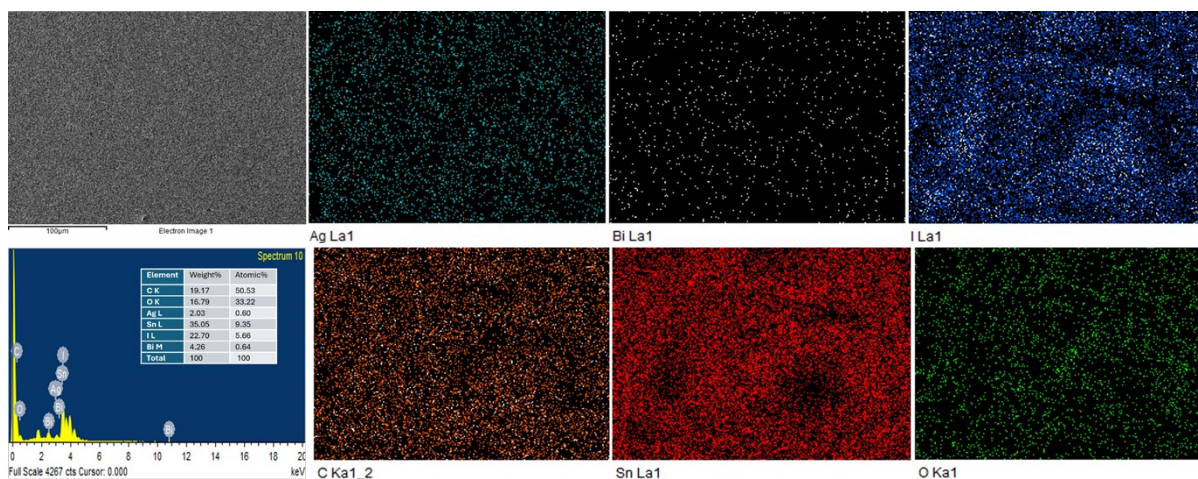
Figure S6. Energy dispersive spectroscopy (EDS). SEM image, elemental mapping, and EDX spectrum of $(BzA)_4AgBiI_8$ double perovskite thin film.

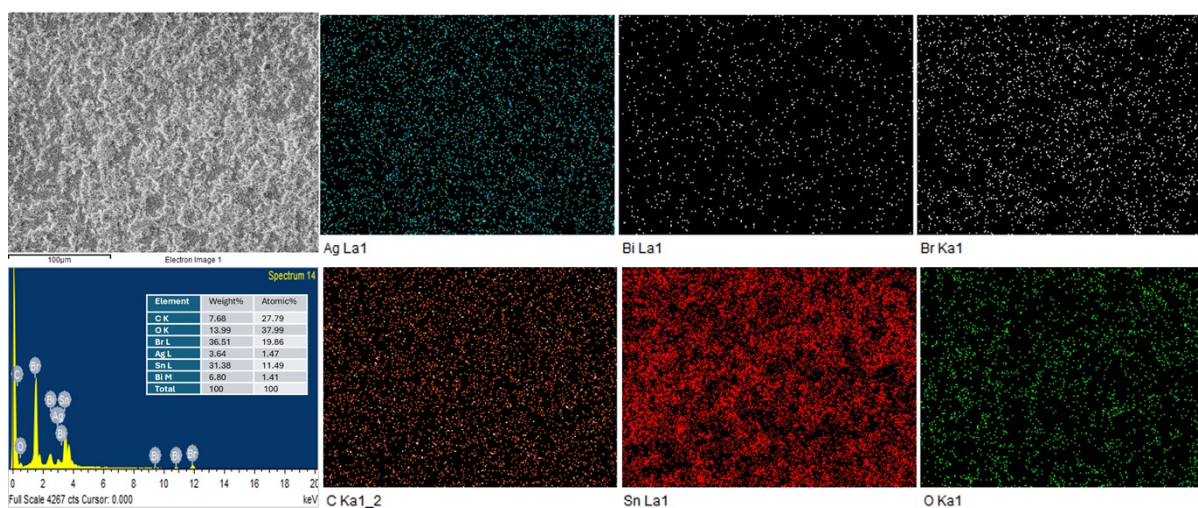**Figure S7**. Energy dispersive spectroscopy (EDS). SEM image, elemental mapping, and EDX spectrum of $(PDMA)_2AgBiBr_8$ double perovskite thin film.

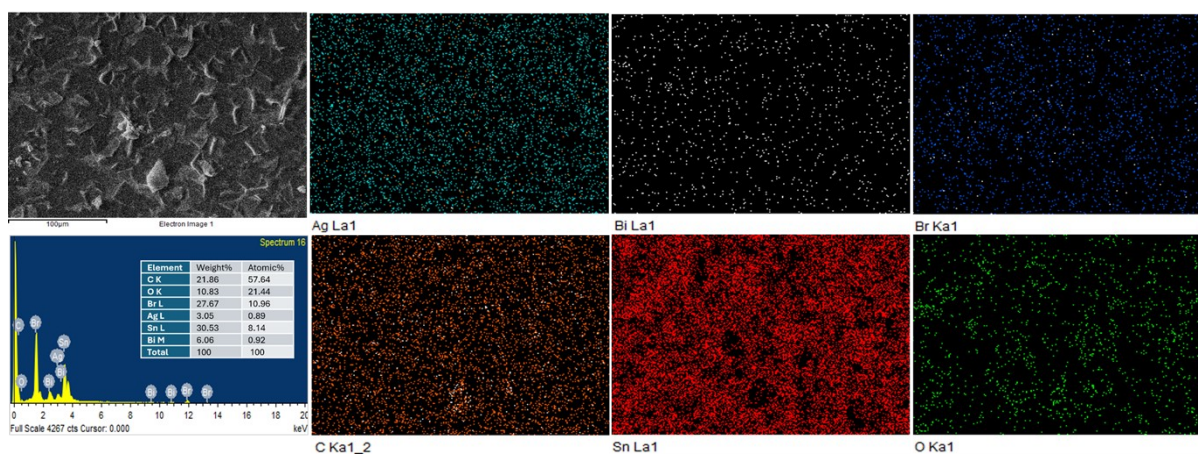**Figure S8**. Energy dispersive spectroscopy (EDS). SEM image, elemental mapping, and EDX spectrum of $(BzA)_4AgBiBr_8$ double perovskite thin film.
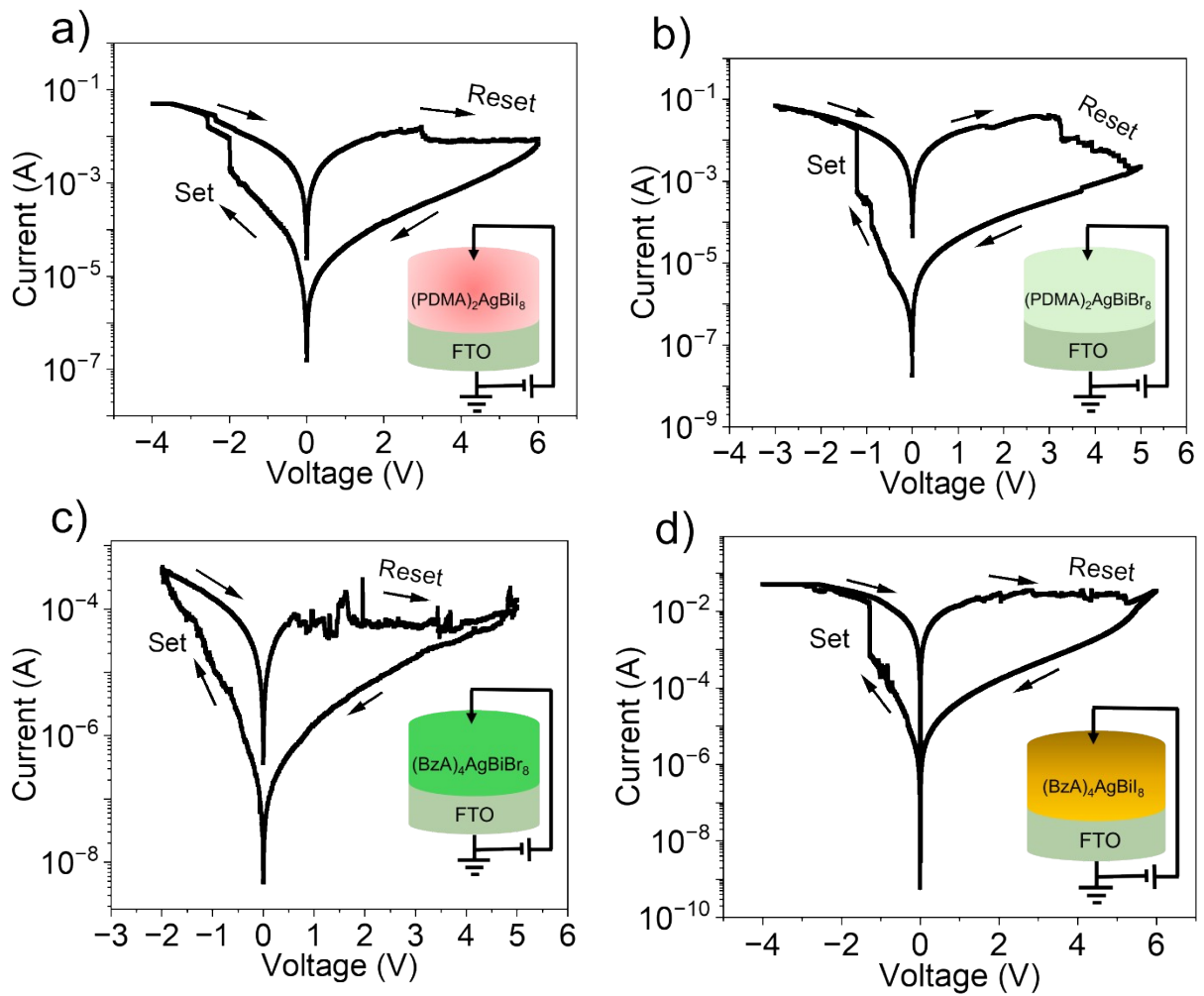
Figure S9. Direct probing of perovskite films a) $(PDMA)_2AgBiI_8$ b) $(PDMA)_2AgBiBr_8$ c) $(BzA)_4AgBiBr_8$ d) $(BzA)_4AgBiI_8$ using a tungsten probe demonstrates intrinsic bipolar resistive switching in all four compositions, confirming that the switching behaviour originates within the perovskite lattice.

Supplementary Discussion 1:

Temperature dependent I-V measurements: Temperature-dependent I–V measurements were performed on the Ag/(BzA)$_4$AgBiBr$_8$/FTO device to probe electronic transport. We clarify an important experimental consideration specific to resistive switching devices. Unlike conventional semiconductor devices, memristive systems inherently exhibit cycle to cycle variability due to stochastic filament formation and ionic redistribution. In many cases, the conductance variations induced by temperature changes are comparable to or even smaller than intrinsic cycle to cycle variations. Due to this inherent variability, obtaining complete switching I-V loops at multiple temperatures is not a reliable way to determine the effect of temperature on electronic transport. This is because it becomes difficult to disentangle temperature effects from stochastic switching variations. To avoid this ambiguity, we restricted the voltage window to the high resistance state (HRS) regime, where no filament formation or ionic redistribution occurs. After systematic testing, we selected a narrow bias range of -0.1 V to +0.1 V (Figure S10a). We note that extending the voltage range to -0.2 V to +0.2 V already induces measurable hysteresis, indicating the onset of ion migration and inducing switching (Figure S10e). In contrast, within ±0.1 V, the I-V curves are fully reversible and hysteresis free, which ensures that the measured current reflects purely electronic transport. Within this controlled low field regime, temperature dependent I-V measurements were performed from room temperature up to 140 °C. At each temperature, the measurement was repeated six times (dual sweep) to ensure reproducibility (Figure S10d), and the current at +0.1 V was extracted for Arrhenius analysis (Figure S10b). The resulting activation energy was found to be approximately 0.072 eV, consistent with shallow electronic trap-assisted conduction in the HRS and confirming that ionic contributions are negligible in this voltage range. In addition, to assess the feasibility of using full switching cycles for temperature dependent analysis, we recorded complete I-V switching loops at only two temperatures, initially at room temperature and again after completing the temperature dependent measurements at 140 °C (Figure S10c). This limited comparison was chosen to evaluate the method's reliability. The resulting I-V characteristics clearly demonstrate that cycle to cycle variability dominates over temperature-induced changes, even when the temperature difference is substantial. The switching voltages, hysteresis width, and current levels vary significantly between cycles, making it impossible to attribute observed differences unambiguously to temperature effects alone. This observation confirms that recording full switching cycles as a function of temperature does not provide a controlled or reliable means of extracting transport parameters in resistive switching devices and further justifies our decision to restrict temperature dependent analysis to the low field, non-switching regime.

While ion-migration-assisted transport was independently probed using time-domain transient measurements under both electrical and optical stimuli, where the evolution and relaxation of conductance after removal of the perturbation were monitored. The long, history-dependent relaxation times observed in these measurements provide direct evidence of ionic motion, complementing the temperature-dependent electronic transport analysis.
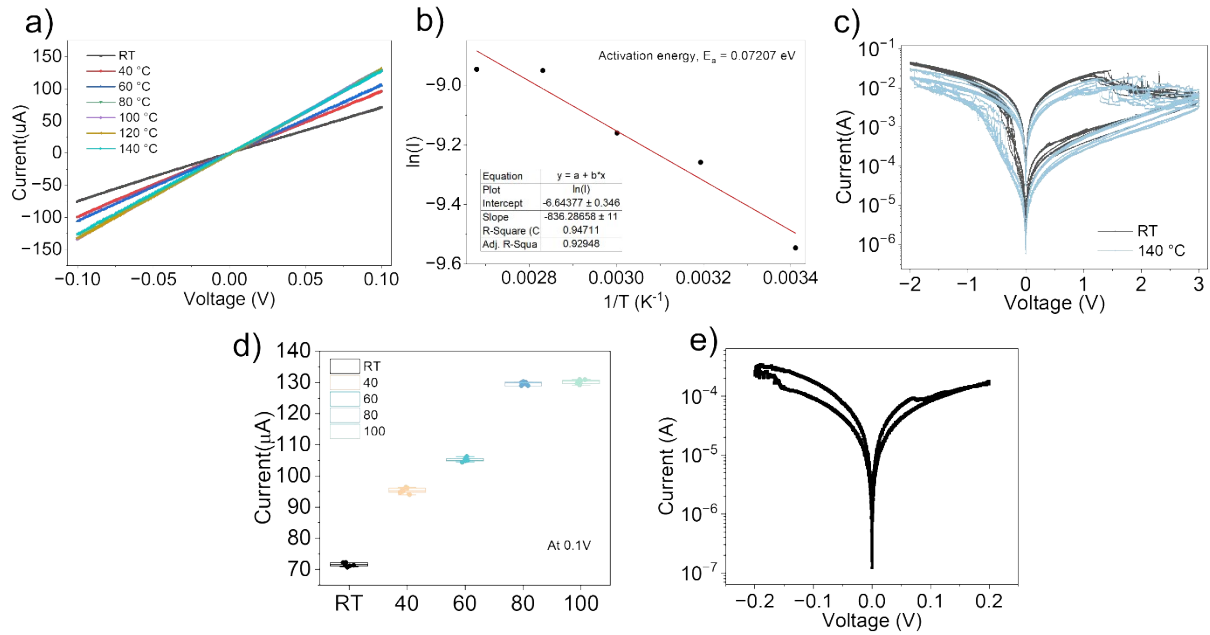
Figure S10. Temperature dependent transport analysis in Ag/(BzA)$_4$AgBiBr$_8$/FTO device. (a) Low field I-V characteristics recorded within the restricted bias window (-0.1 V to +0.1 V. The bias window was selected to limit the data acquisition to the HRS with no resistive switching or ionic movement occurring. (b) Arrhenius analysis derived from the current at +0.1 V, yielding an activation energy of 0.072 eV, consistent with thermally activated electronic transport. (c) Full switching I-V cycles were measured at room temperature and 140 °C, showing cycle to cycle variability that limits reliable temperature dependent extraction from complete loops. (d) Repeated low field dual sweep I-V measurements at representative temperatures. (e) I-V characteristics acquired over a large bias range (-0.2 V to +0.2 V), showing measurable hysteresis indicative of incipient ion migration.
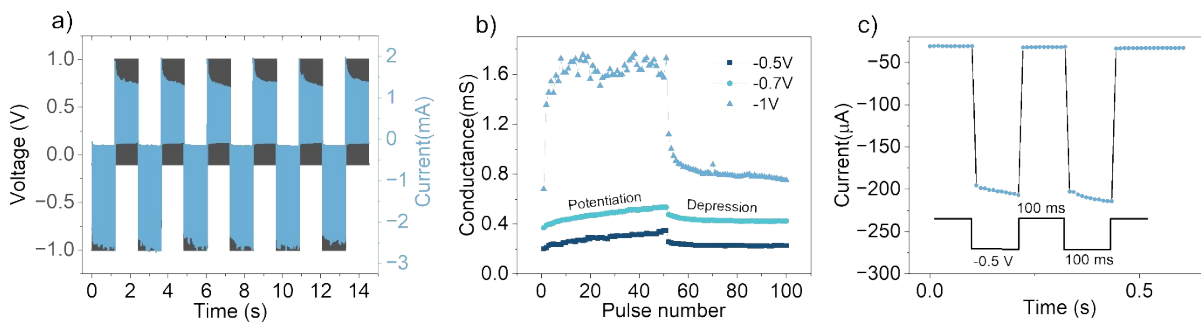

Figure S11. Synaptic behaviour in Ag/(BzA)$_4$AgBiBr$_8$/FTO device a) Increase and decrease in current (blue) upon application of 50 negative and positive voltage (black) pulses respectively with consecutive six cycles (600 pulses) to demonstrate reliable and reproducible potentiation and depression. b) PPF response at 0.1 s pulse width. c) Pulse amplitude dependant plasticity.
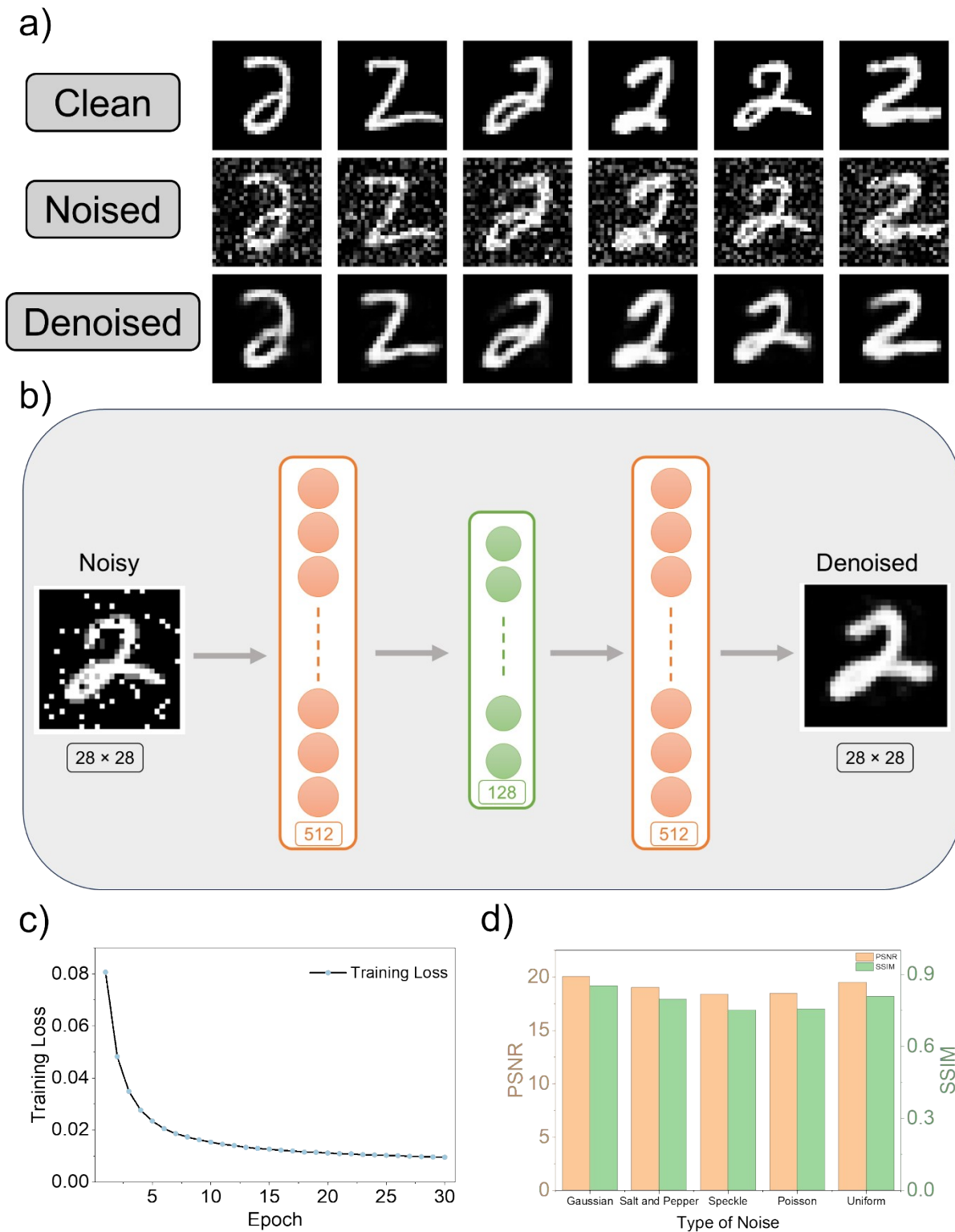
Figure S12. Denoising of an image through a device-aware autoencoder model. a) Example of denoising of MNIST digits (Gaussian noise model). b) Schematic representation of autoencoder network. c) Loss vs Epoch curve for denoising. d) Different noise models used with performance quantified using peak signal-to-noise ratio (PSNR) and structural similarity index measure (SSIM).

Supplementary Discussion 2:

Denoising: A device-aware denoising autoencoder was developed to see whether the synaptic weights obtained through experimental testing were suitable for neuromorphic image restoration of MNIST digits. To assess model robustness, denoising was performed under several noise models at an intensity of $\sigma = 0.3$, with performance quantified using peak signal-to-noise ratio (PSNR) and structural similarity index measure (SSIM), metrics that respectively evaluate reconstruction accuracy at the pixel level and preservation of structural image features relative to the reference image.

Table S1: Comparison of different noise models used with performance quantified using MSE, MAE, PSNR and SSIM.

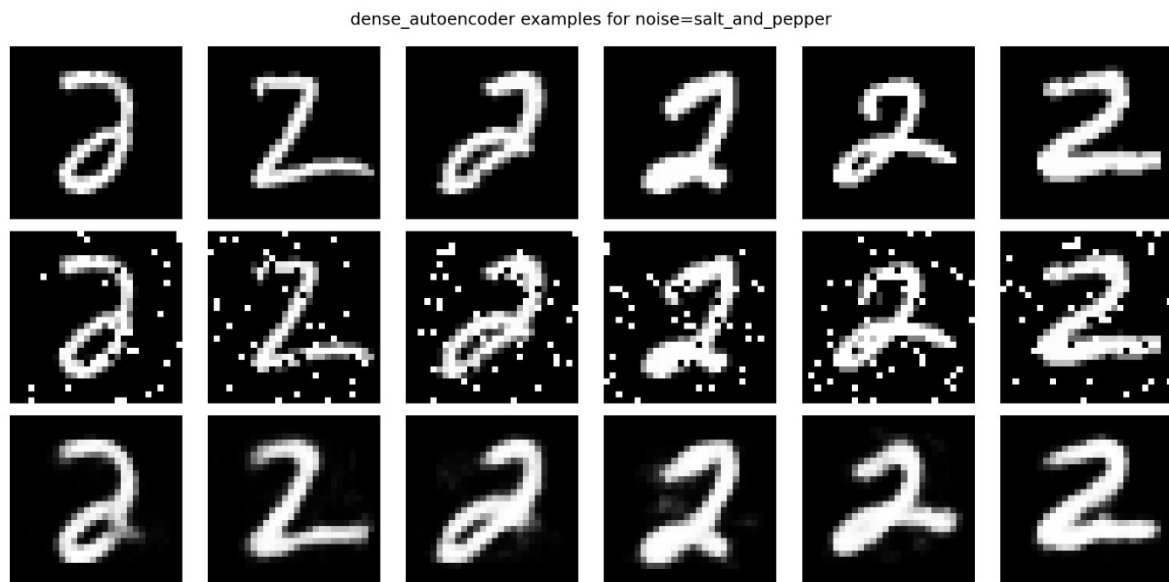| Noise Model	MSE	MAE	PSNR	SSIM
Gaussian	0.010745	0.037876	20.03516	0.850682
Salt and Pepper	0.013717	0.04551	19.02748	0.795678
Speckle	0.01571	0.053309	18.3877	0.751527
Poisson	0.015456	0.052696	18.45718	0.754813
Uniform	0.012356	0.043278	19.50634	0.808233

Figure S13. Denoising of image through device aware autoencoder model (Salt and Pepper).
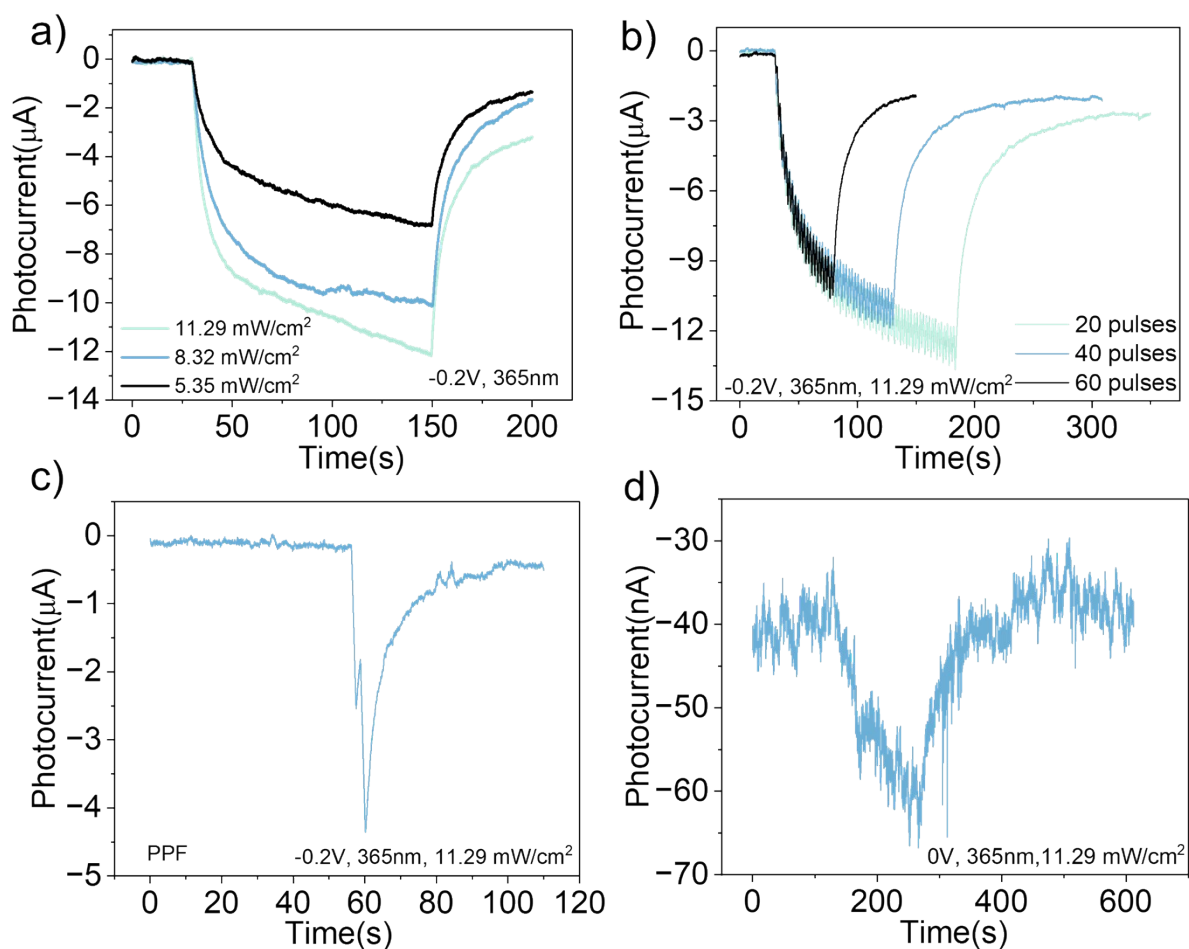
Figure S14. Optical synaptic behavior in the $Au/(BzA)_4AgBiBr_8/FTO$ memristor device. (a) Photo response under continuous UV exposure (365 nm) at -0.2 V, showing a gradual increase in current with increasing light intensity. (b) Pulse number-dependent optical response under UV illumination (365 nm, 11.29 mW/cm^2) at -0.2 V, demonstrating cumulative conductance modulation. (c) Paired-pulse facilitation (d) Photo response under continuous UV exposure (365 nm) at 0V, showing a gradual increase in current.
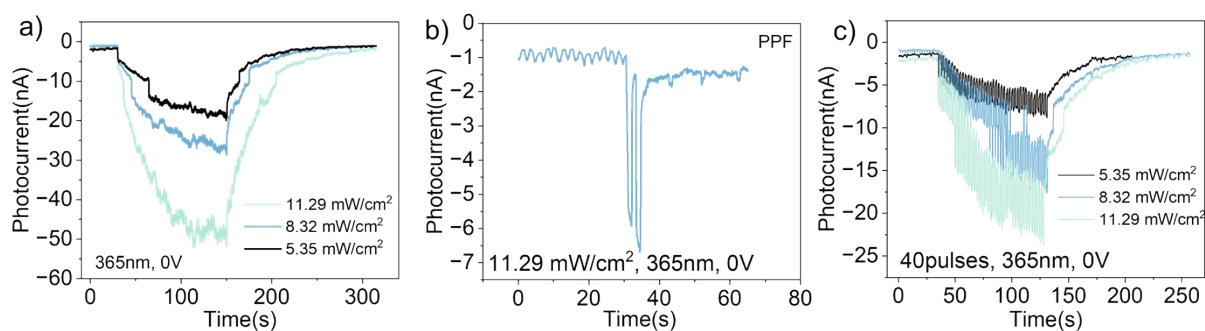

Figure S15. Optical synaptic behavior in the $Au/Spiro-OMeTAD/(BzA)_4AgBiBr_8/SnO_2/FTO$ device at zero bias. (a) Photo response under continuous UV exposure (365 nm), showing a gradual increase in current with increasing light intensity. (b) Paired-pulse facilitation (c) Pulse intensity-dependent responses recorded with 40 light pulses (365 nm) at zero bias.
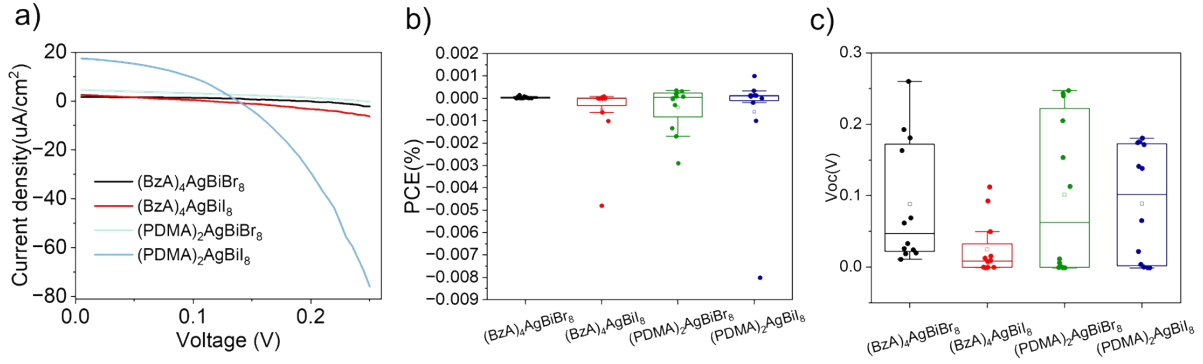
Figure S16. Limited photovoltaic performance of the lead-free double perovskite solar cell devices with spin-coated SnO_2 ETL layer: (a) J-V curve, (b) power conversion efficiency (PCE), and (c) open-circuit voltage.
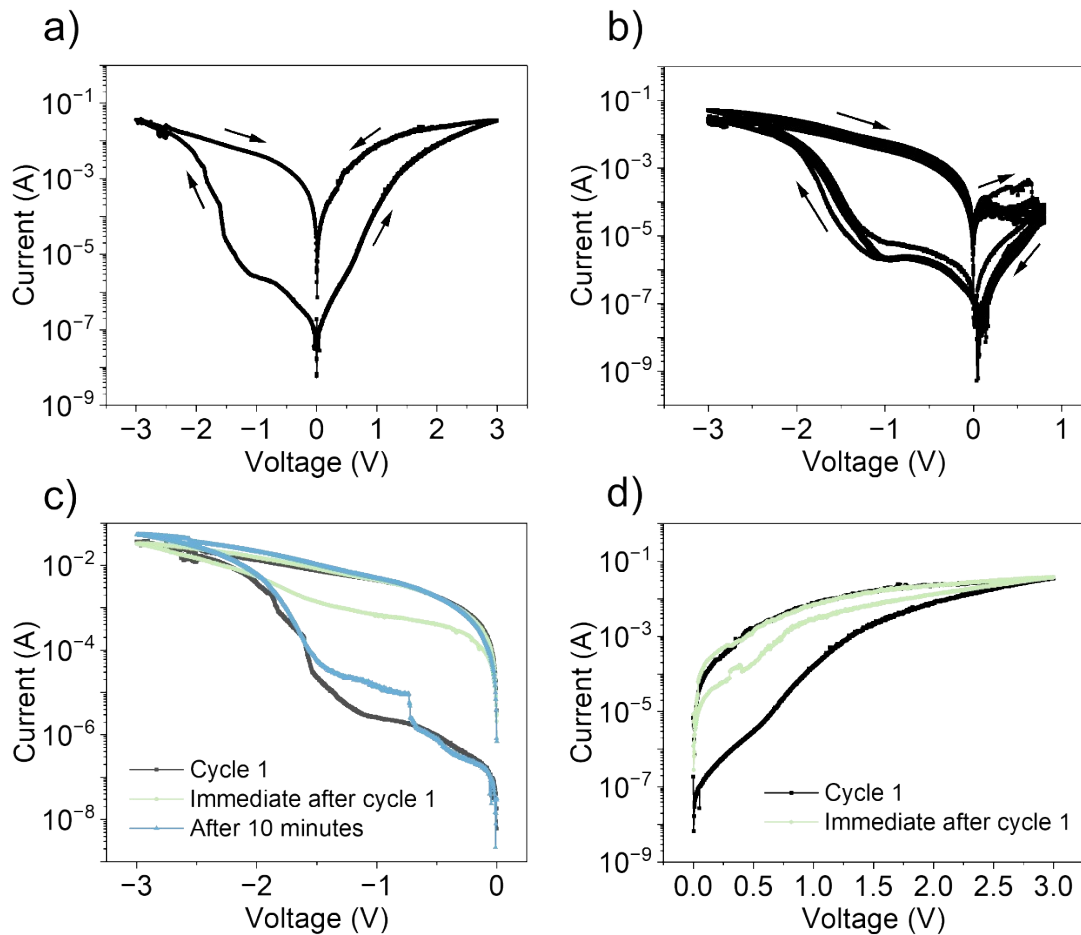
Figure S17. Volatile resistive switching behavior in Au/Spiro-OMeTAD/(PDMA)$_2$AgBiI$_8$/SnO$_2$/FTO device with spin-coated SnO$_2$. a) Switching characteristics under both positive and negative voltage sweeps. b) application of small (+0.8 V) positive sweep instantaneously returns device to HRS c) Negative sweep-induced switching: the device remains in LRS when immediately remeasured and returns to HRS after ~10 min. d) Positive sweep-induced switching: the device remains in LRS when immediately remeasured.

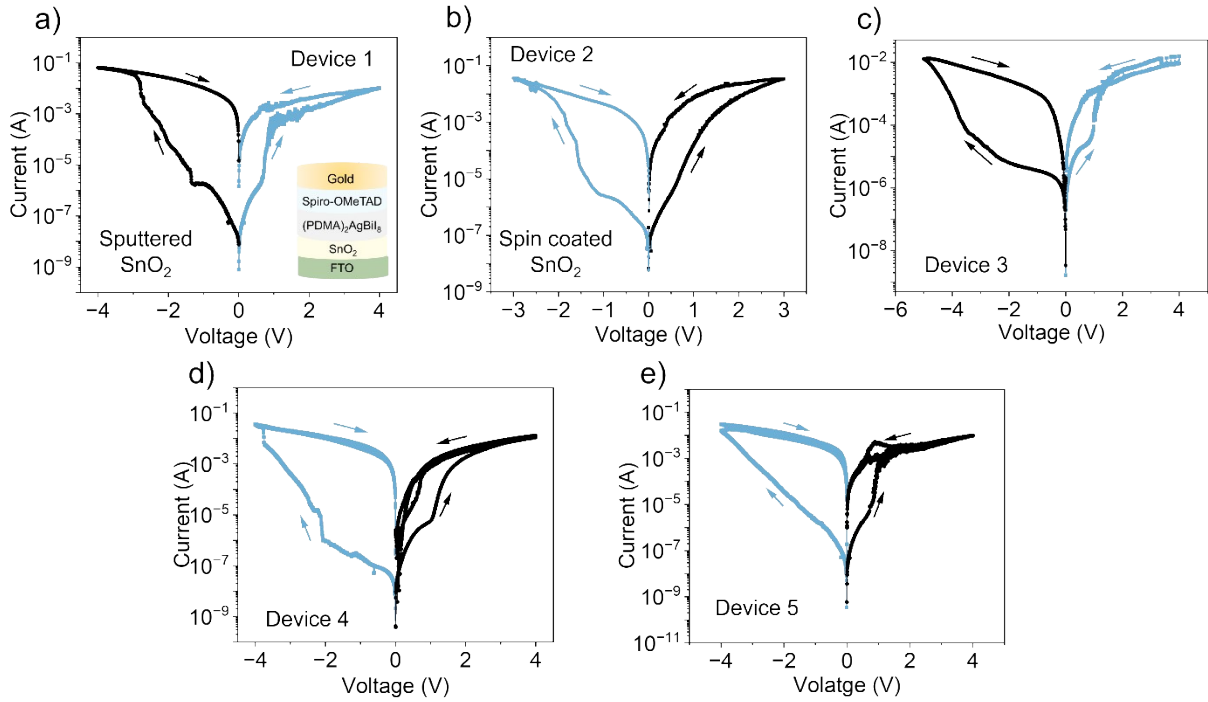**Figure S18.** Electrical characteristics measured from five nominally identical Au/Spiro-OMeTAD/(PDMA)$_2$AgBiI$_8$/SnO$_2$/FTO devices, demonstrating reproducibility of the observed volatile resistive switching behavior

Synaptic behavior in Au/Spiro-OMeTAD/(PDMA)$_2$AgBiI$_8$/SnO$_2$/FTO solar cell device
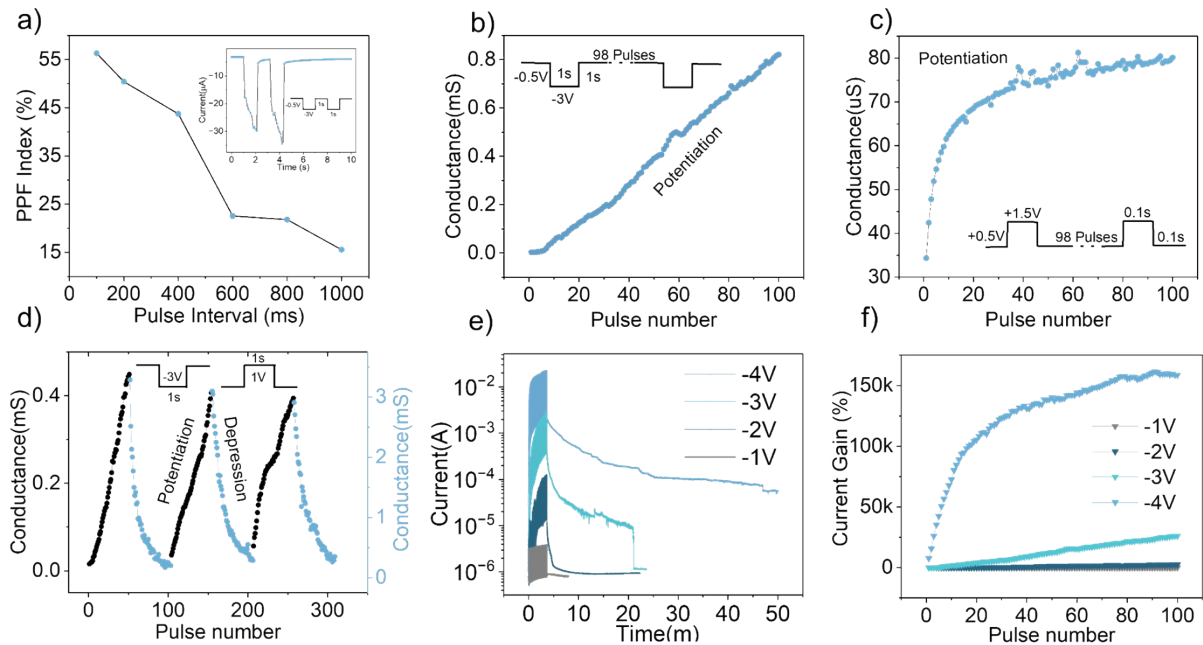
Figure S19. Synaptic behavior in Au/Spiro-OMeTAD/(PDMA)$_2$AgBiI$_8$/SnO$_2$/FTO solar cell device. (a) Decrease in PPF index with increasing pulse width, inset shows PPF response at 1 s pulse width. (b) Potentiation achieved through 100 consecutive negative pulses (-3 V amplitude). (c) Depression achieved through 100 consecutive positive pulses (+1.5 V amplitude). (d) Reversible potentiation and depression using 50 negative (-3 V) and 50 positive (+1 V) pulses repeated over three cycles (total of 300 pulses), demonstrating reliable plasticity. (e) Relaxation dynamics following 50

pulses of varying amplitudes (-1 V to -4 V), showing increased relaxation time with higher amplitude. (f) Amplitude-dependent current gain under 100 negative pulses (-1 V to -4 V), highlighting enhanced synaptic weight change with increasing stimulus strength.

Supplementary Discussion 3:

To assess the neuromorphic potential of volatile system based on Au/Spiro-OMeTAD/(PDMA)$_2$AgBiI$_8$/SnO$_2$/FTO solar cell configuration, synaptic behavior was explored by analyzing the response to voltage pulses. When two successive voltage pulses (-3V) were applied, the conductance response to the second pulse was higher than that of the first, demonstrating a classic paired-pulse facilitation (PPF) effect. The PPF index, defined as the ratio of the conductance change induced by the second pulse relative to the first, was found to decrease as the interval between pulses increased, from 100 ms to 1000 ms, demonstrating that the facilitation effect weakens as the interval grows longer, reflecting the temporal dynamics of ion redistribution (**Figure S18**a).

This facilitation can be attributed to the residual ionic displacement from the first pulse, which reduces the threshold for conduction upon the second stimulus, mimicking short-term synaptic memory behavior. When 100 consecutive voltage pulses were applied, a progressive increase in conductance was observed, indicative of potentiation, which is a key feature of synaptic plasticity. This potentiation effect was evident under both negative (-3 V, 1 s) and positive (+1.5 V) pulse trains (Figure 6b,c). Furthermore, when 50 positive pulses (+1 V, 1 s) were applied following 50 negative pulses (-3 V, 1 s), a decrease in conductance was recorded, representing synaptic depression (Figure 6d). This trend aligns with earlier observations where applying a small positive voltage after a negative SET facilitated a rapid return to the HRS, supporting the notion of field-assisted relaxation. However, when higher amplitude positive pulses were used following negative ones, the device exhibited potentiation instead, suggesting that stronger fields may promote additional ion migration, thereby enhancing conductance rather than reversing it.

The underlying mechanism is likely to involve field-driven halide and Ag ion migration, as negative pulses displace Ag$^+$ ions towards the top electrode and I$^-$ ions toward the bottom electrode, creating I vacancies and Ag accumulation near the top electrode, resulting in a steady increase in conductance. Conversely, positive pulses induce reverse ion migration, moving Ag$^+$ and I$^-$ ions back, thereby reducing the device conductance, corresponding to depression. If the positive voltage is sufficiently high, it may create new vacancies or reinforce existing ones, leading to renewed filament formation and potentiation. Furthermore synaptic weight change, or current gain, was found to be strongly dependent on the amplitude of the applied voltage pulses.[3] Devices were stimulated using both single pulses and a series of 100 pulses, with a width of 1s and an inter-pulse interval of 1s, while varying the pulse amplitude from -1 V to -

4 V (Figure S19). The excitatory postsynaptic current (EPSC) was recorded at a constant read bias of -0.5 V. With amplitudes of -1 V, no notable conductance change was detected, indicating the stimulus was below the threshold for effective ion migration. It was shown that higher pulse amplitudes (-2 V, -3 V, and -4 V) led to a pronounced increase in both peak EPSC and current gain (defined as the percentage increase in current relative to the initial state), for both single and multiple pulse stimulations. In addition to enhanced peak response, higher amplitude pulses resulted in slower decay dynamics, indicating improved short-term memory retention. This underscored the role of pulse amplitude in modulating synaptic weight and establishing memory retention, aligning well with bioinspired synaptic behavior.

A similar trend was observed by increasing the number of pulses at a fixed amplitude. When -3 V pulses (1 s width) were applied in sets of 1, 2 and 100, a progressive enhancement in peak EPSC and current gain was recorded with an increasing number of pulses. These results confirm that the strength and duration of stimuli (in terms of number and amplitude of pulses) significantly modulate the synaptic response, mimicking biological activity-dependent plasticity.[4] Such synaptic behavior in lead-free halide perovskite devices, including both electrical and optical responses, highlights their multifunctionality and adaptability to diverse external stimuli.
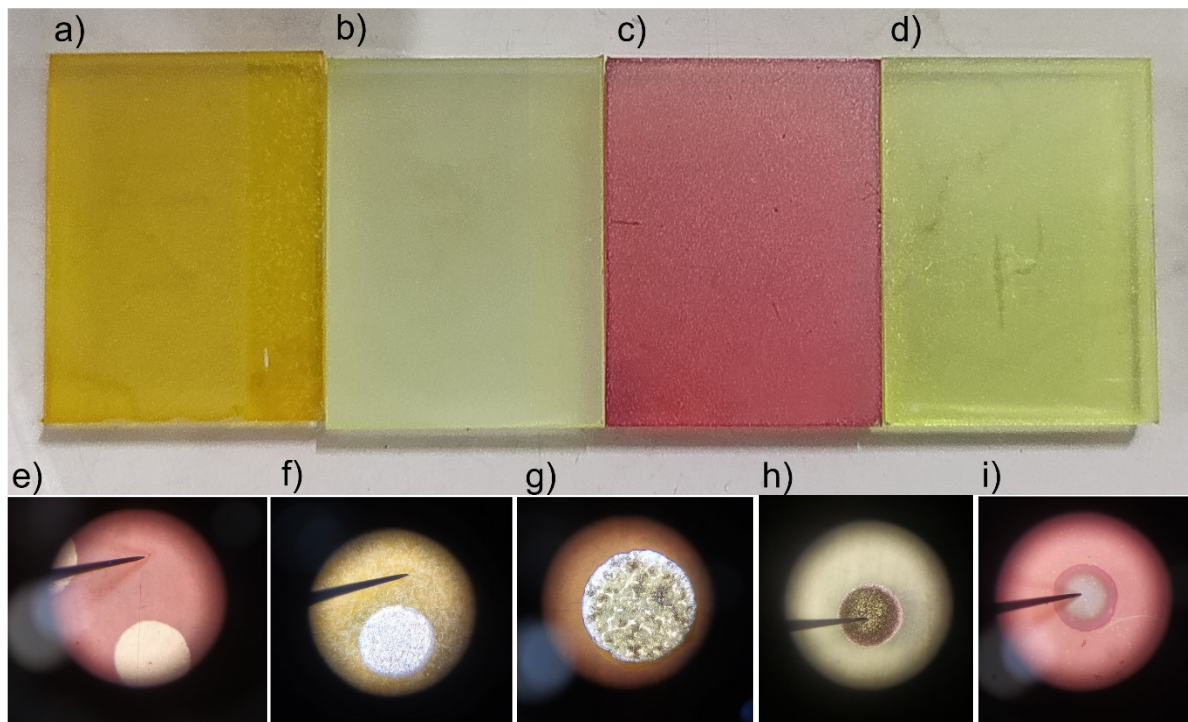

Figure S20. Optical images of (a) $(BzA)_4AgBiI_8$ (b) $(PDMA)_2AgBiBr_8$ (c) $(PDMA)_2AgBiI_8$ and (d) $(BzA)_4AgBiBr_8$ thin films. (e-i) Al and Ag electrode degradation on double perovskite thin films (e) fresh Au electrode (f) fresh Ag electrode (g-h) degraded silver electrodes (i) partially disappeared Ag electrode.
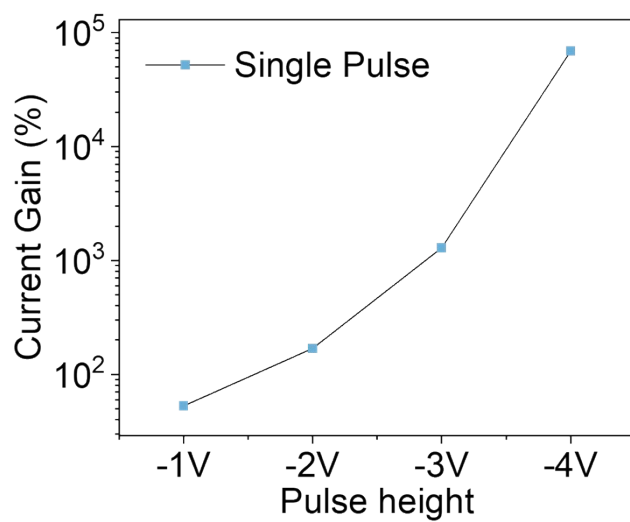
Figure S21. Current gain in the Au/Spiro-OMeTAD/(PDMA)$_2$AgBiI$_8$/SnO$_2$/FTO device with increase in amplitude.

Table S2. Comparison of this work with previous studies on halide perovskite based memristive devices.

Device configuration	Non-volatile switching	Volatile switching	Electrical synapse	Optical synapse	Computing task	Light sensing	Self-powered	Layered structure	Lead free	Ref.
Ag/BCP/PCBM/ (FAMA)$_{0.91}$Cs$_{0.05}$Rb$_{0.04}$Pb (I$_{0.85}$Br$_{0.15}$)$_3$ /Perfluoroarene/ PTAA/ITO	Yes	-	-	-	-	-	-	-	-	5
Au/Ag/PMMA/OIHP:Ag /ITO/PEN	-	Yes	Yes	-	-	-	-	-	-	6
Ag/AgI/ MAPbBr$_3$/ PEDOT: PSS/FTO	Yes	Yes	-	-	-	-	-	-	-	7
Ag/CsPbBr$_3$/pTPD/ PEDOT: PSS/ITO	Yes	Yes	-	-	Reservoir computing	-	-	-	-	8
Au/ Cs$_2$CO$_3$/ BA$_2$Pb$_{0.5}$Sn$_{0.5}$I$_4$/ PEDOT:PSS/ITO	-	Yes	Yes	-	Digit recognition	-	-	Yes	-	9
Ag/BCP/PCBM/ FAPbI$_3$/NiO$_x$/ITO	-	-	-	Yes	Image recognition		Yes	-	-	10
Ag/PMMA/AgBiI$_4$/FTO	Yes	-	Yes	-	Image recognition	-	-	-	Yes	11
Au/Cs$_2$AgBiBr$_6$/ZnO/Au (Lateral)	-	-	-	Yes	Pattern recognition	Yes	-	-	Yes	12
Ag or Au/Spiro-OMeTAD/(PDMA)$_2$AgBiX$_8$/SnO$_2$/FTO	Yes	Yes	Yes	Yes	Denoising	Yes	Yes	Yes	Yes	This work

References

[1] (a) M. M. Ganaie, G. Bravetti, S. Sahu, M. Kumar, J. V Milić, *Mater. Adv*. **2024**, 5, 1880.

   (b) M. Ghasemi et al. *ChemPhysChem.* **2026**, e202500764.

[2] D.J. Kubicki, M. Saski, S. MacPherson, K. Gałkowski, J. Lewiński, D. Prochowicz, J. J. Titman, S. D. Stranks, *Chem. Mater.* **2020**, 32, 8129.

[3] J. Shi, S. Kang, J. Feng, J. Fan, S. Xue, G. Cai, J. S. Zhao, *Nanoscale Horiz.* **2023**, 8, 509.

[4] J. Gong, H. Yu, X. Zhou, H. Wei, M. Ma, H. Han, S. Zhang, Y. Ni, Y. Li, W. Xu, *Adv. Funct. Mater.* **2020**, 30, 2005413.

[5] M. Loizos, K. Rogdakis, W. Luo, P. Zimmermann, A. Hinderhofer, J. Lukic, M. Tountas, F. Schreiber, J.V. Milic, E. Kymakis, *Nanoscale Horiz.* **2024**, 9, 1146.

[6] L. Tang, J. Wang, Y. Huang, H. Wang, C. Wang, Y. Yang, *J. Mater. C.* **2024**,*12,* 3622-3631.

[7] N.K. Pendyala, C. Gonzales, A. Guerrero, *Small Structures*, **2025**, *6*, 2400380.

[8] R.A. John, Y. Demirağ, Y. Shynkarenko, Y. Berezovska, N. Ohannessian, M. Payvand, P. Zeng, M.I. Bodnarchuk, F. Krumeich, G. Kara, I. Shorubalko, *Nat. Commun*. **2022,** 13, 2074.

[9] L. Chen, S. Saleh, F. Tavormina, L. Di Mario, J. Li, Z. Xie, N. Masciocchi, C. J. Brabec, B. Koldehofe, M. A. Loi, *Adv. Mater.* **2025**, 2414430.

[10] W. Huang, J. Tang, B. Li, X. Zhang, Z. Lin, H. Zhang, P. Hang, X. Yu, X.A. Li, and L. Wang, *Small*, p.2505327, 2025.

[11] H. Ye, Z. Liu, H. Han, T. Shia and G. Liao, *Mater. Adv.*, 2022, **3**, 7248-7256.

[12] Z. Cheng, T. Wang, J. Zhu, Y. He, S. Liu, M.Y. Li, H. Lu, X. Wen, J. Lee, S. Liu, S. Mao, *Small,* 2025, 21, 2411129.